# Electrostatic fields for the control of evaporating charged fuel sprays

Daniel Fredrich [*], Erik Weiand, Andrea Giusti

*Imperial College London, Exhibition Rd, London SW7 2AZ, UK*

## ARTICLE INFO

## ABSTRACT

The current socio-economic shift towards electrification of the transport sector and development of hybrid thermal–electric propulsion systems provides new opportunities for the development of 'clean' aviation technologies. In this work, the use of electrostatic fields to control the location of electrically charged fuel droplets is proposed as a novel technology to enhance pre-evaporation of liquid sprays in confined spaces. An electrospray in cross-flow is numerically investigated using large-eddy simulations for a range of flow and droplet conditions in order to study the feasibility of the approach. A deterministic model is further introduced to compute the trajectory of single droplets in a steady cross-flow. This enables a separation of the effects of turbulence, droplet repulsion and evaporation through comparison with data obtained from the large-eddy simulations, and at the same time provides a cheap computational tool to explore a wider range of operating conditions. It is shown that external electrostatic fields below the breakdown threshold of air can significantly change the trajectory of charged droplets at moderate flow velocities. Moreover, electrostatic forces acting in the opposite direction of the mean cross-flow can potentially be used to stabilise the spray position within a confined region, hence allowing for an increase of the residence time available for full evaporation. The application and modulation of such electrostatic forces is envisioned as a new paradigm to achieve '*targeted evaporation*' in next-generation hybrid thermal–electric aero-engines and to improve the fuel-oxidiser mixing quality. The electrical power associated with the external electrostatic field to achieve droplet stabilisation is negligible compared to the thermal power released by complete combustion of the injected fuel. In addition, it is shown that stabilisation of the droplets enhances the evaporation rate (by more than 30%) and mixing quality due to an increase of the relative velocity between the droplets and the gas flow, as well as the turbulence induced by the stagnating spray cloud. The results of this work offer new insights for the development of advanced fuel injection strategies based on electrohydrodynamics.

## 1. Introduction

Recent advances in the field of aerospace science and technology show significant progress towards carbon-neutral air transportation. To achieve this ambitious goal, research groups in both industry and academia are pursuing various strategies from the use of zero-carbon fuels (Masri, 2021) to fully electrical propulsion systems (Brelje and Martins, 2019). However, each strategy presents its own set of unique challenges. The anticipated transition to hydrogen-powered aircraft (Brewer, 2017; Baroutaji et al., 2019) faces a number of complex issues related to the sustainable and economically feasible production of hydrogen, as well as its specific infrastructure and on-board storage requirements. Technical solutions are furthermore needed to ensure safe combustor operation with hydrogen flames and to minimise the impact of increased in-flight water vapour emissions. All-electric aircraft, on the other hand, are not expected to be a viable option for long-range commercial flights considering the relatively low specific

energy density of current battery technologies (Gnadt et al., 2019). The use of liquid sustainable aviation fuel (SAF) appears to be the most promising short to intermediate term solution for a reduction of carbon dioxide emissions (Zhang et al., 2016). SAFs are produced from sustainable feedstocks and renewable resources and have the potential to reduce lifecycle emissions by up to 80% compared with traditional aviation fuel (International Air Transport Association). Hence, the next generation of aero-engines is still expected to involve the consumption of liquid fuels; with lean premixed prevapourised systems currently considered the target for low-emission combustion (Liu et al., 2017).

State-of-the-art aeronautical combustors achieve low emission levels by controlling the mixing between fuel and air. This requires complex designs of the air streams and fuel injectors, often involving a compromise between the different requirements for fuel preparation and flame stabilisation. To ensure safety, reduce pressure losses and at the same time maintain a compact design, kerosene is typically injected in the

---

vicinity of the primary reacting region. The fuel preparation relies on advanced injection systems capable of accomplishing a fine atomisation (i.e., sprays with high surface area-to-mass ratios) and consequently fast evaporation. Sprays are often injected into relatively high-speed swirling flows, which are responsible for the stabilisation of the flame by creating a recirculation region, in addition to droplet transport and fuel–air mixing (in airblast injectors, air co-flows also control the spray atomisation (Lefebvre and McDonell, 2017)). In practical configurations, the residence time of the droplets before reaching the flame is very limited making the requirements for fast evaporation and mixing the main target for the development of low-emission injection systems. In reality, complete premixing is never achieved and liquid droplets often reach the reacting region resulting in increased emission levels.

In the search for improved control of the spray characteristics and location, electrically charged fuel sprays (called here: electrosprays) have received increased attention in recent years. So far mainly studied in the context of diesel fuels, e.g., for direct injection spark ignition engines (Shrimpton and Laoonual, 2006) and liquid fuels in mesoscale combustors (Kyritsis et al., 2002; Walther and Ahn, 2011; Higuera and Tejera, 2017), electrosprays offer a degree of spray 'tuning' further downstream of the injector (Ahmed et al., 2021a,b). Increased droplet evaporation rates are attained via a mechanism based on electrostatic fragmentation (or fission), where each droplet disintegrates into multiple smaller sibling droplets once it reaches the Rayleigh limit for droplet stability (Rayleigh, 1882; Doyle et al., 1964; Shrimpton, 2005). In addition, electric repulsion forces between the equally charged droplets can lead to increased inter-droplet separation (Crowley, 1995; Shrimpton and Yule, 1999), thus promoting droplet dispersion and fuel–air mixing. Two different approaches for generating electrosprays have been proposed in the past. First, so-called charge injection atomisers can be employed to induce electric charges directly into a dielectric fluid (such as kerosene or SAFs) using a high voltage power supply (Kelly, 1984; Shrimpton, 2009; Kourmatzis and Shrimpton, 2014). Second, highly conductive additives (e.g., nanoparticles) can be suspended into the liquid base fuel to 'dope' its electrical conductivity (Tang and Gomez, 1996; Kyritsis et al., 2004), creating what is often referred to as a nanofluid (or nanofuel). Nanofuels are a key element of modern combustion research due to their potential in reducing an engine's specific fuel consumption and pollutant emissions, see e.g., Mehta et al. (2014).

The present work explores the use of electrosprays in combination with external electrostatic fields to add flexibility to the design space of future aero-engines. In particular, externally imposed electrostatic fields are envisioned as a means for modulating the trajectories of charged fuel droplets independently of the flow configuration. Such mechanism would allow increased control over the evaporation process, i.e., the location of the fuel vapour release with a successive impact on the fuel–air mixing quality, the flame behaviour and the formation of pollutants. Broadly similar technologies involving the control of charged particles or liquids using electrostatic fields have previously been investigated in the field of electrohydrodynamics (EHD). Some of these technologies are already well established in industry-relevant applications such as electrostatic precipitation (Yamamoto and Velkoff, 1981; Soldati, 2000; Mizeraczyk et al., 2013), powder coating (Bailey, 1998) and ink-jet printing (Galliker et al., 2012).

The introduction of hybrid thermal–electric propulsion systems (Brelje and Martins, 2019) in the civil aviation sector could make a future deployment of EHD technologies in aeronautical combustion devices increasingly feasible due to the availability of electrical energy on board. In this context, the current work aims to investigate the characteristics of a kerosene electrospray under the influence of electrostatic fields. A liquid jet in cross-flow, sometimes also referred to as spray in cross-flow, is the chosen test configuration representing a flow arrangement widely encountered in many practical and canonical combustion applications, see e.g., Mongia (2003) and Fredrich et al.

(2022), respectively. The particular concept proposed in the present work is an electrospray in cross-flow (ESICF). Such ESICF combines the application of an external electrostatic field with a spray of electrically charged fuel droplets injected perpendicularly into a bulk flow of air.

The specific objectives of this work are: (*i*) to study the modulation of the spray trajectory using a range of electrostatic fields and bulk flow velocities; (*ii*) to investigate the use of electrostatic forces to increase the residence time available for droplet evaporation over a finite-length mixing region. For this purpose, large-eddy simulations (LES) are performed and a simple deterministic model is devised to complement the LES results. The competing effects of the drag force induced by the bulk flow versus the external electrostatic force are examined. The increase of the residence time is accomplished by adjusting the orientation of the electrostatic field to obtain a force opposite to the bulk flow drag. In general, it is to be demonstrated that the proposed ESICF configuration can provide control over the location of the fuel vapour release – a concept introduced here as '*targeted evaporation*'. Subsequent effects on the combustion process, i.e., the flame dynamics and the formation of pollutants, will be further investigated in future work. The paper is organised as follows. First, the methods are introduced, followed by the results and their discussion. A summary and conclusions close the paper.

## 2. Methods

### 2.1. Large-eddy simulation

A LES method with Eulerian–Lagrangian formulation and two-way coupling for dilute sprays (Jenny et al., 2012) is applied. The method is based on the open-source CFD software package OpenFOAM and solves the Favre-filtered transport equations for mass, momentum, energy and species conservation using second-order accurate schemes. The sub-grid scale stress tensor is closed by the constant Smagorinsky model. Only drag (Putnam, 1961) and electrostatic forces are assumed to act on the droplets, and the effect of sub-grid scale fluctuations on the droplet motion is neglected. The widely-used rapid mixing model (Miller et al., 1998; Aggarwal et al., 1984) is employed to evaluate the evaporation rates. It should be noted that other evaporation models are also available, such as the Abramzon–Sirignano model (Abramzon and Sirignano, 1989), which includes the effects of Stefan flow, as well as models that consider non-equilibrium effects at the gas–liquid interface. The choice of evaporation model is not expected to change the main outcomes of this work, but should be investigated in the future.

The electrostatic forces are computed from the electrostatic potential, $\varphi$, solved in the Eulerian framework. Following Gauss's law, $\varphi$ can be expressed as a Poisson equation according to:

$$\nabla^2 \varphi = -\frac{\rho_q}{\varepsilon_0}, \tag{1}$$

where $\rho_q$ is the local charge density evaluated in each finite volume cell of the computational mesh and $\varepsilon_0$ is the vacuum permittivity (see e.g., Lawton and Weinberg, 1969). The local electrostatic field, $\boldsymbol{E}$, can be directly computed from the gradient of the potential field:

$$\boldsymbol{E} = -\nabla \varphi. \tag{2}$$

The electrostatic force, $\boldsymbol{F}_{E,i}$, acting on the $i$th charged droplet is then given by:

$$\boldsymbol{F}_{E,i} = q_{d,i}\,\boldsymbol{E}. \tag{3}$$

As previously justified in Doyle et al. (1964), the net charge, $q_{d,i}$, of each spherical droplet is considered constant throughout the droplet lifetime, i.e., there is no electrical discharge via transfer of charge into the gas phase. This assumption is based on the charge decay rate (see e.g., Li et al., 2021), which can be estimated to be orders of magnitude
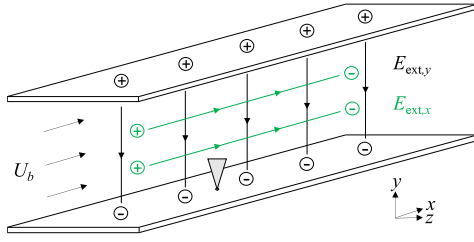
**Fig. 1.** Schematic of the ESICF configuration indicating external electrostatic fields in the negative $y$-direction (black field lines — Case A) and positive $x$-direction (green field lines — Cases B and C). The origin of the frame of reference is located at the centre of the bulk flow inlet boundary plane. (For interpretation of the references to colour in this figure legend, the reader is referred to the web version of this article.)

**Table 1**
Range of parameters investigated throughout this work.

| Parameter | Case A | Case B | Case C |
|---|---|---|---|
| $T_{g,0}$ [K] | 300 | 700 | 700 |
| $d_{0,i}$ [μm] | $\in \{5{:}95\}$ | 25, 50, 75 | $\in \{5{:}95\}$ |
| $\theta_d$ [°] | $\pm 9$ | 0 | $\pm 9$ |
| $|\boldsymbol{u}_{d,0}|$ [m/s] | 30 | 10 | 10 |
| $U_b$ [m/s] | 2, 20, 80 | 10 | 10 |
| $\mathrm{Re}_{b,\max}$ | $5 \times 10^5$ | $1.5 \times 10^4$ | $1.5 \times 10^4$ |
| $\mathrm{We}_{\max}$ | 21.0 | 3.3 | 4.2 |
| $E_{\mathrm{ext}}/E_{\mathrm{ref}}$ | $-0.1$, 0, $\pm 1$ | 0, 2 | 0, 2 |
| Orientation | $y$-axis | $x$-axis | $x$-axis |

slower than the droplet evaporation rates observed in the present work. The droplet net charge is given by:

$$q_{d,i} = \rho_{q,d,i}\, V_{d,i}, \tag{4}$$

where $V_{d,i}$ and $\rho_{q,d,i}$ are the volume and charge density of the $i$th droplet, respectively. The initial charge density, $\rho_{q,d,0}$, is assumed equal for all droplets.

It should be noted that in the current modelling framework, repulsion forces between droplets located in the same computational cell cannot be accounted for (since these forces are computed from the potential field). This introduces some uncertainty with respect to the droplet dispersion. However, for the cases investigated in the present work, the maximum repulsion force experienced between each droplet pair never exceeds the external electrostatic force acting on the respective individual droplets. In fact, for 99.9% of all droplets, the force induced by the external electrostatic field was calculated to be at least one order of magnitude higher than the repulsion force and the global average was always more than two orders of magnitude higher. Crucially, the influence of repulsion forces between droplets located in different cells is captured by the modelling with reasonable accuracy.

### 2.2. Computational setup

The configuration investigated in this work consists of a channel flow between two parallel plates with a fuel spray injected from the bottom plate. The simulated channel geometry with a length of 0.3 m and a cross sectional area of $0.1 \times 0.1$ m$^2$ is shown in Fig. 1. The computational domain is spatially discretised using a structured mesh of about $3 \times 10^6$ hexahedral cells with edge lengths between 0.3 and 1.5 mm. The grid points are refined in close proximity to the top and bottom boundaries, which are treated as adiabatic no-slip walls. Periodic conditions are applied at the left and right boundaries. Three different case setups (A, B and C) are considered to address the two objectives of this work. The main differences between the three cases are the orientation of the external electrostatic field and the properties of the incoming bulk air flow and fuel spray, as summarised in Table 1. A constant bulk flow velocity, $U_b$, with a flat profile is prescribed at the cross-flow inlet to mimic the air supply from a large plenum. The cross-flow consists of pure air at atmospheric pressure, $p_{g,0} = 101{,}325$ Pa, with a temperature of $T_{g,0} = 300$ K (Case A) or 700 K (Cases B and C, where evaporation is studied).

The transverse spray is injected at $x = 0.12$ m, either perfectly perpendicular or in the form of a solid cone with an opening angle of $\theta_d = \pm 9°$. The liquid fuel mass flow rate is $\dot{m}_f = 0.06$ g/s. It should be noted that although conventional kerosene fuel is investigated in the current work, the ESICF concept presented here is equally relevant for the use of liquid SAFs (Al-Nuaimi and Kyritsis, 2019). Both monodisperse and polydisperse droplet size distributions are studied. For the latter, a Rosin–Rammler distribution is assumed to compute the initial droplet diameters, $d_{0,i}$, using a mean diameter of $d_{0,\mathrm{mean}} = 50$ μm and

a dispersion parameter equal to $q = 4$. The initial droplet temperature is $T_{d,0} = 300$ K in all cases. The injection velocity magnitude, $|\boldsymbol{u}_{d,0}|$, is reported in Table 1. Electrostatic fields are imposed by applying a constant external potential difference, $\Delta\varphi_{\mathrm{ext}}$, between two opposing parallel domain boundaries with a distance $L$. The resulting external electrostatic field strength, $|E_{\mathrm{ext}}| = \Delta\varphi_{\mathrm{ext}}/L$, is kept below the theoretical electrical breakdown threshold of ambient air ($E_{\mathrm{bd}} = 3 \times 10^6$ V/m; see e.g., Uhm (1999)) in all cases. For conciseness, a reference value of $E_{\mathrm{ref}} = E_{\mathrm{bd}}/3$ is defined here. Finally, a constant initial droplet charge density of $\rho_{q,d,0} = -1$ C/m$^3$ is assumed (only for cases where $E_{\mathrm{ext}} \neq 0$ V/m) to compute the net charge of each droplet (Shrimpton, 2009; Rigit and Shrimpton, 2009). This is a conservative value, since charge densities of $-10$ C/m$^3$ from state-of-the-art EHD atomisers have already been reported in the literature (Shrimpton and Laoonual, 2006).

### 2.3. Deterministic model

A two-dimensional (2D) deterministic model is furthermore introduced as a computationally inexpensive tool for the approximation of single droplet trajectories. The formulation presented here is specific to a uniform external electrostatic field and a constant bulk flow with a flat velocity profile. The model is based on Newton's second-law applied to a single non-evaporating droplet:

$$\frac{\mathrm{d}\boldsymbol{u}_d}{\mathrm{d}t} = \frac{1}{m_d}(\boldsymbol{F}_D + \boldsymbol{F}_E), \tag{5}$$

where $\boldsymbol{u}_d$ is the droplet velocity, $t$ is the time and $m_d$ is the mass of the droplet. Only the drag and electrostatic forces are considered, consistent with the LES implementation. The drag force can be written as:

$$\boldsymbol{F}_D = 0.125\, \rho_g\, \boldsymbol{u}_{\mathrm{rel}}\, |\boldsymbol{u}_{\mathrm{rel}}|\, C_D\, \pi\, d^2, \tag{6}$$

where $d$ is the droplet diameter and $\rho_g$ denotes the density of the gas phase. $\boldsymbol{u}_{\mathrm{rel}}$ is the relative velocity between the horizontal bulk flow and the droplet. The drag coefficient, $C_D$, can be evaluated from Refs. (Yuen and Chen, 1976; Wallis, 2020):

$$C_D = \begin{cases} 0.424, & \text{if } \mathrm{Re}_d > 1000, \\ \frac{24}{\mathrm{Re}_d}\left(1 + \frac{\mathrm{Re}_d^{2/3}}{6}\right), & \text{otherwise}, \end{cases} \tag{7}$$

based on the droplet Reynolds number $\mathrm{Re}_d = \rho_g\, |\boldsymbol{u}_{\mathrm{rel}}|\, d/\mu_g$, where $\mu_g$ is the dynamic viscosity of the gas phase. Note that in the limit of very low $\mathrm{Re}_d$, Stokes' law is invoked using $C_D = 24/\mathrm{Re}_d$. Finally, the electrostatic force can be written as:

$$\boldsymbol{F}_E = q_d\, \frac{\Delta\varphi_{\mathrm{ext}}}{L}\, \hat{\boldsymbol{e}}_L, \tag{8}$$

where $\hat{\boldsymbol{e}}_L$ is the unit vector normal to the two opposing parallel domain boundaries (direction of the electrostatic field) used to impose the external electrostatic potential difference. After application of the boundary conditions, i.e., the droplet injection location and velocity, the term $\mathrm{d}\boldsymbol{u}_d/\mathrm{d}t$ is integrated in time to obtain the evolution of the droplet position and velocity.
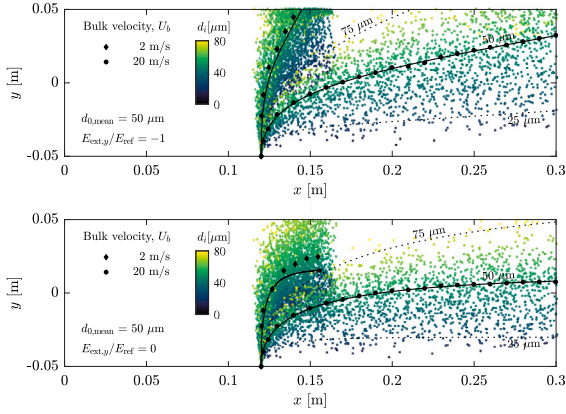
**Fig. 2.** Instantaneous droplet size and spatial distribution after 20 ms of injection obtained from LES including evaporation for different bulk flow velocities. Top: external electrostatic field in the negative *y*-direction. Bottom: no electrostatic forces. Black symbols indicate the respective bin averages conditioned on $d_i = 50\pm1$ μm. Solid and dotted lines represent the corresponding deterministic model predictions for several droplet diameters (25, 50 and 75 μm) and a black square marks the final droplet position after 20 ms of injection. – Case A.

## 3. Results and discussion

### 3.1. Modulation of droplet trajectories

An external electrostatic field is first applied in the negative *y*-direction between the top and bottom plate (Case A). The flow field was simulated for 60 ms of physical time before injecting the fuel droplets for a duration of 20 ms. The droplet distribution for two different bulk flow velocities is shown in Fig. 2 and compared to a case without the influence of any electrostatic forces. The downwards pointing external electrostatic field clearly has an impact on the spatial droplet distribution at both $U_b = 2$ and 20 m/s. The negatively charged droplet cloud moves closer to the top plate resulting in less bending of the spray's mean trajectory, which was calculated from spatial bin averages conditioned on a droplet diameter of $d_i = 50\pm1$ μm. This effect is more pronounced at the lower value of $U_b$. Results from the 2D deterministic model ($d = 50$ μm) are also included in the form of solid lines for validation purposes. In both cases, the deterministic model predictions are in good agreement with the bin-averaged LES data, suggesting the modelling framework is applicable to represent droplet transport under the influence of drag and electrostatic forces. The small underprediction of the vertical droplet penetration is to be expected, since in contrast to the LES, the two-way coupling between the dispersed and continuous phase is not accounted for in the deterministic model.

The droplet trajectories are a result of the competing effects of the drag and electrostatic forces. Assuming Stokes' regime (similar conclusions are found by considering the actual drag force), the ratio of the magnitude of the electrostatic and drag forces is:

$$\frac{|\boldsymbol{F}_E|}{|\boldsymbol{F}_D|} = \frac{d^2\,|\rho_{q,d}|\,|\Delta\varphi_{\text{ext}}|}{18\,L\,\mu_g\,|\boldsymbol{u}_{\text{rel}}|}. \qquad (9)$$

If the strength of the external electrostatic field, the droplet charge density and the gas-phase properties are kept constant, then an increase of the relative velocity in the direction of the electrostatic field with increasing droplet diameter is expected towards reaching an equilibrium between the two forces (terminal velocity). This explains the higher vertical velocity component for larger droplets observed in Fig. 2.

It is also clear that the initial drag force increases with increasing bulk flow velocity with an impact on the droplet trajectories. Fig. 3 shows the droplet trajectories computed from the deterministic model by varying the external electrostatic field strength and direction, and
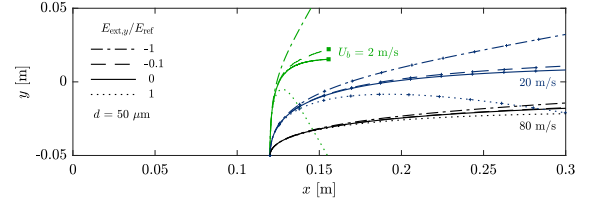


**Fig. 3.** Single droplet trajectories obtained from the deterministic model for different bulk flow velocities and external electrostatic fields applied in the *y*-direction. Square symbols mark the final droplet position after 20 ms of injection – Case A.
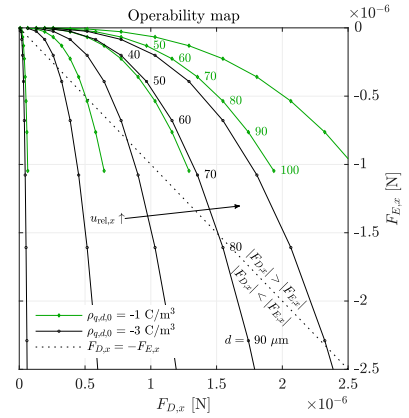


**Fig. 4.** Operability map of the drag and electrostatic forces acting on a single non-evaporating droplet in the diameter range from 10 to 100 μm. Relative velocities of 2, 20, 40, 60 and 80 m/s (from left to right) were considered and $E_{\text{ext},x}/E_{\text{ref}} = 2$.

using bulk flow velocities of 2, 20 and 80 m/s. These velocities correspond to bulk flow Reynolds numbers of $\text{Re}_b = \rho_g\,U_b\,h/\mu_g = 1.25 \times 10^4$, $1.25 \times 10^5$ and $5 \times 10^5$, and maximum Weber numbers of $\text{We}_{\text{max}} = \rho_g\,|\boldsymbol{u}_{\text{rel}}|^2\,d/\sigma = 2.7$, 4.6 and 21.0, respectively, where $h$ is the channel height and $\sigma$ is the surface tension calculated based on Beaton and Hewitt (1989). For the combination of the highest $\text{Re}_b$ number and strongest external electrostatic field, a relative vertical deviation of only $\pm4$ mm from the default $E_{\text{ext},y} = 0$ trajectory is observed at $x = 0.3$ m. It can therefore be concluded that the sensitivity of the mean droplet trajectory to $E_{\text{ext},y}$ decreases considerably with increasing $U_b$.

Conventional aero-engine injectors require high relative velocities between the fuel and air streams to improve the liquid film breakup, as well as moderately high bulk flow velocities to increase the turbulence levels for droplet evaporation and fuel-oxidiser mixing. It is obvious that at such high velocities, the effectiveness of any externally applied electrostatic field becomes almost negligible. However, it may be possible to achieve improved fuel-oxidiser mixing without the need for high Re number flows by exploiting electrostatic forces at moderate bulk flow velocities. One such strategy is proposed in the following.

### 3.2. Quasi-infinite droplet residence times

Instead of applying an external electrostatic field in the vertical direction, the field orientation is now assumed to be aligned with the cross-flow. In a realistic setup, this would present an obvious challenge as the solid electrode plates would block off the fluid flow. Actual technical solutions could involve a diagonal electrostatic field arrangement, an S-shaped channel geometry or the use of electrically conducting grids (Kyritsis, 2020), e.g., a flow conditioner, thereby introducing some pressure losses. The aim of the proposed streamwise configuration is to utilise electrostatic forces to keep fuel droplets stationary in the absolute frame of reference — by counteracting the drag force induced
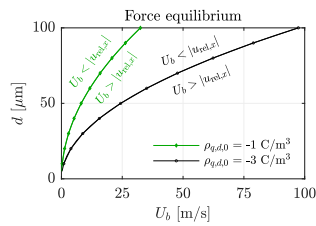
**Fig. 5.** Force equilibrium line between the drag and electrostatic forces (where $U_b = u_{\text{rel},x}$) as a function of the bulk flow velocity and droplet diameter. Results were obtained from calculations of a single stationary non-evaporating droplet using $E_{\text{ext},x}/E_{\text{ref}} = 2$.
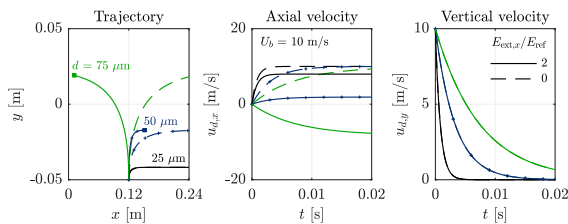


**Fig. 6.** Single droplet trajectories and axial & vertical velocities obtained from the deterministic model for a number of droplet diameters. Note that some of the solid and dashed lines are overlapping. – Case B.



**Fig. 7.** Instantaneous distribution of the droplet location and axial & vertical velocities obtained from LES without evaporation. Lines indicate the deterministic model predictions for a droplet with $d = 50$ μm. – Case B.



**Fig. 8.** Instantaneous droplet location and age obtained from LES including evaporation for (a) an external electrostatic field of $E_{\text{ext},x}/E_{\text{ref}} = 2$ in the streamwise direction and (b) no electrostatic forces. – Case B.

by the bulk flow. This will essentially increase the droplet residence time without the need for a longer mixing section.

Simple calculations based on Stokes' law were performed to evaluate the relationship between the drag force and the electrostatic force in such streamwise configuration. For this purpose, a range of droplet diameters, charge densities and relative velocities between the droplet and the bulk flow were considered. The resulting operability map for a given electrostatic field strength ($E_{\text{ext},x}/E_{\text{ref}} = 2$) is shown in Fig. 4. Each line in the map was obtained from Eq. (9) by varying the droplet diameter while keeping the droplet charge density and the relative velocity fixed. Note that a bulk flow temperature of 700 K was assumed to emulate preheated air conditions. For a given droplet charge density and a given relative velocity, the ratio $|F_{E,x}|/|F_{D,x}|$ generally increases with increasing droplet diameter, thus making the electrostatic force more effective. Conversely, an increase of the relative velocity decreases the effectiveness of the externally applied electrostatic field. Higher droplet charge densities can furthermore extend the operating limits significantly. A diagonal line indicates equilibrium between the drag and electrostatic forces in the direction of the electrostatic field ($F_{D,x} = -F_{E,x}$). Note that in order to obtain a stationary droplet (i.e., the absolute droplet position remains constant), the bulk flow velocity must equal the relative velocity indicated in Fig. 4 along the force equilibrium line.

The corresponding operating points to achieve stationary droplets as a function of the bulk flow velocity and droplet diameter are further shown in Fig. 5. Similar maps can be produced for any other electrostatic field strength and droplet charge density. Fig. 5 can be used to estimate the bulk flow velocity that stabilises droplets with a constant diameter. For example, at a charge density of $-3$ C/m³, a 50 μm droplet is stabilised at a bulk flow velocity of approximately 25 m/s. For a lower charge density of $-1$ C/m³, a lower bulk flow velocity of just under 10 m/s is required to stabilise the same 50 μm droplet (conditions of Case B). Any operating condition above the force equilibrium line, i.e., lower $U_b$ or higher $d$, leads to an upstream movement of the droplet induced by a more dominant electrostatic force, whereas the region below this line implies downstream convection of the droplet due to a stronger drag force. It should be noted here that the results in Fig. 4 and Fig. 5 are based on the use of Stokes' law for drag. More accurate evaluations across the whole range of droplet Reynolds numbers can
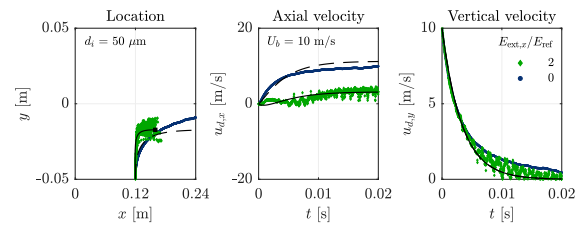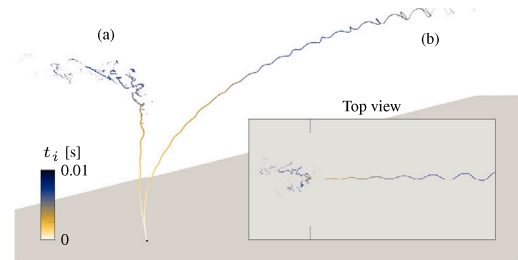
be obtained by using a more general drag force formulation (this is left for future studies).

Based on the above calculations, the deterministic model was employed to obtain adequate parameters for an ESICF system with near quasi-infinite droplet residence times — Case B. Three different droplet diameters are considered with a fixed vertical injection velocity of 10 m/s. The trajectory, axial velocity and vertical velocity of the single droplets are shown in Fig. 6, computed for a duration of 20 ms of physical time. This time is estimated to be slightly longer than the actual lifetime of similar-sized evaporating kerosene droplets under such conditions (Fredrich and Giusti, 2022). Stabilisation of the droplet position is obtained for a diameter of 50 μm and an external electrostatic field strength of $E_{\text{ext},x}/E_{\text{ref}} = 2$. Note that for a given charge density, the electrostatic force increases with increasing droplet diameter. For droplets larger than a certain size threshold, the electrostatic force overcomes the drag force in the flow direction and the droplets are transported upstream against the bulk flow (cf. Fig. 5). It should be noted that due to the streamwise orientation of the external electrostatic field, the droplets' vertical velocity is not significantly impacted. Nevertheless, larger droplets penetrate the cross-flow closer to the top plate due to their higher initial momentum. The individual trajectories observed for the different droplet sizes can also be used as an indicator for the behaviour of polydisperse sprays.

The above conditions were simulated in LES using a monodisperse spray with $d_i = 50$ μm and, initially, no evaporation (evaporation effects are examined in the next section). Fig. 7 shows the corresponding droplet characteristics. Under the influence of the external electrostatic field, an almost stationary droplet cloud with axial velocities near zero is obtained. In addition, increased droplet dispersion is achieved as a result of two main effects. First, higher relative velocities between the droplets and the bulk flow cause higher local $Re_d$ numbers and higher turbulence intensities in the continuous phase. Second, repulsion forces between the equally charged droplets lead to stronger inter-droplet separation. To quantify the increase in dispersion, the droplets' deviation from the mean trajectory was computed in a number of spatially discrete bins and averaged over the total number of droplets. The standard deviation is found to increase fourfold from 1.1 mm to 4.4 mm under the influence of electrostatic forces.
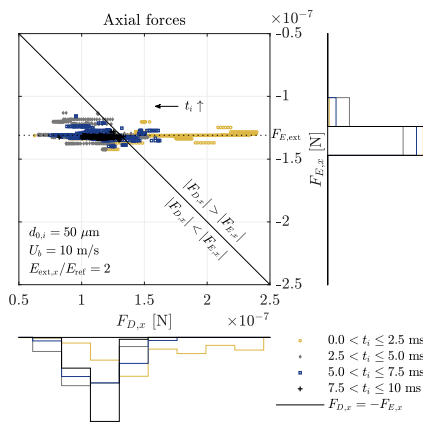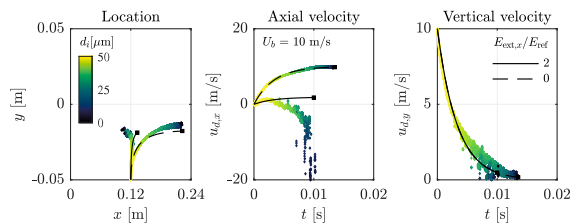
**Fig. 9.** Comparison of the axial drag and electrostatic forces for an instantaneous droplet cloud (grouped by age) obtained from LES including evaporation. Marginal histograms have been added and a dotted line indicates the constant droplet force, $F_{E,\text{ext}} = -1.31 \times 10^{-7}$ N, induced by the external electrostatic field. – Case B.



**Fig. 10.** Instantaneous distribution of the droplet location and axial & vertical velocities obtained from LES including evaporation. Lines indicate the deterministic model predictions for a droplet with $d = 50$ μm. – Case B.



**Fig. 11.** Instantaneous distribution of the droplet size, relative velocity and Reynolds number versus the droplet age obtained from LES including evaporation. – Case B.



**Fig. 12.** Instantaneous fuel vapour mass fraction, $Y_f$, in the mid-plane and in an axial plane obtained from LES including evaporation. Top: external electrostatic field in the $x$-direction. Bottom: no electrostatic forces. The corresponding droplet distribution is coloured by the axial droplet velocity, $u_{d,x,i}$, and was sampled in the range $\pm 5 \times 10^{-4}$ m perpendicular to the mid-plane. – Case B.

### 3.3. 'Targeted evaporation' – control over the local fuel vapour release

The evaporation characteristics of the proposed streamwise configuration are investigated in this section. The simulations were run for two flow-through times after droplet injection (equivalent to 60 ms of physical time) and the results presented below were obtained after an additional two flow-through times. Fig. 8 shows a three-dimensional representation of the instantaneous droplet location and age. Without the inclusion of any electrostatic forces, the fuel droplets follow the bulk flow and evaporate while being convected downstream. However, once the external electrostatic field is applied, the spray behaviour changes drastically. The droplets become almost stagnant and evaporate in a stationary region just above the injection location. As already discussed, this behaviour is caused by a balance between the axial drag force and the axial electrostatic force, represented by a diagonal line in Fig. 9. Note that any deviations from the external electrostatic force, $F_{E,\text{ext}} = q_{d,i} E_{\text{ext},x}$ — constant in monodisperse sprays under the constant net charge assumption (Doyle et al., 1964) — represent the effects of the repulsion forces. The sum of the scalar product of $\boldsymbol{F}_{E,\text{ext}}$ and the droplets' velocity vector indicates the electrical power required for droplet stabilisation, which was calculated to be about five orders of magnitude lower than the thermal power available from the supplied fuel (estimated as the product of the lower heating value and mass flow rate of the fuel). As the droplets evaporate, the influence of the drag force reduces considerably and the older droplets are transported upstream. Shortly before complete evaporation, the smallest droplets undergo a rapid acceleration in the negative axial direction as shown in Fig. 10. This is due to the assumption that the droplet charge is conserved while the diameter decreases. Therefore, the same electrostatic force exerted on the droplets requires a higher relative velocity to reach a balance between the drag and electrostatic forces.
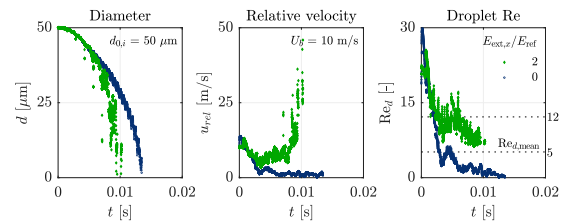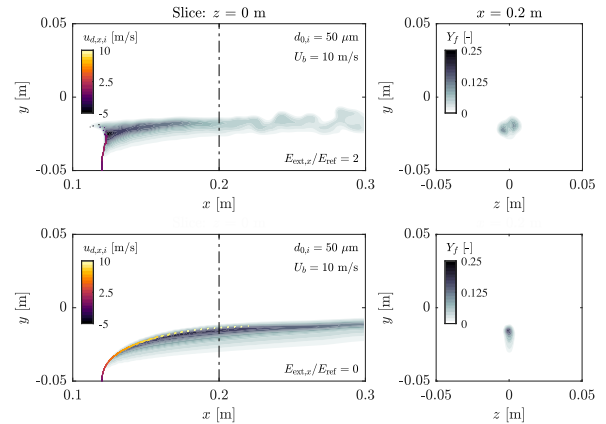
It is noteworthy that in the specific case of a nanoparticle-laden liquid, i.e., a nanofuel, a constant, non-zero terminal diameter is reached when the nanoparticles form a solid shell on the droplet surface (Wei et al., 2016). Assuming a uniform distribution of nanoparticles suspended into the liquid base fuel, the pre-defined terminal diameter can be exploited for increased fluid control. This concept presents an interesting direction to be explored in future research.

Fig. 11 shows three additional droplet quantities to further analyse the influence of the electrostatic force on the overall spray characteristics. The most obvious effect is a reduction of the total evaporation time from 13.5 ms to just over 10 ms (>30%) compared to the case with no electrostatic field. In practice, this reduction is expected to be even greater due to a secondary droplet breakup mechanism not accounted for in the present work. During evaporation, droplet surface instabilities on the gas–liquid interface are amplified by the conserved electric charge resulting in enhanced atomisation via electrostatic fission (Yule et al., 1995) once the Rayleigh limit (Rayleigh, 1882) is reached. Evaporation models including electrostatic fission have been proposed in the literature (Kourmatzis, 2017; Ahmed et al., 2018) and will be incorporated in future work.

The enhanced evaporation rate observed here is a direct effect of the higher relative velocity (also quantified in Fig. 11), which leads to an increase of the mean $Re_d$ number by 140% from 5 to 12 (horizontal dashed lines). The quicker evaporation process further promotes the complete pre-evaporation of the fuel within a confined region. The effect on the mixing is shown in Fig. 12, through the instantaneous fuel vapour mass fraction in the mid-plane and in an axial plane ($x = 0.2$ m) for the cases with and without electrostatic forces. The corresponding instantaneous droplet locations within $\pm 5 \times 10^{-4}$ m perpendicular to the mid-plane are visualised for reference, coloured by their axial velocity. Comparison of the two axial slices reveals a wider, more uniformly distributed fuel vapour distribution with lower
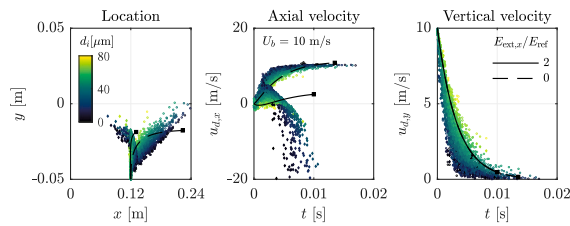
**Fig. 13.** Instantaneous distribution of the droplet location and axial & vertical velocities obtained from LES including evaporation for a polydisperse spray. Lines indicate the deterministic model predictions for a droplet with $d = 50$ μm. – Case C.
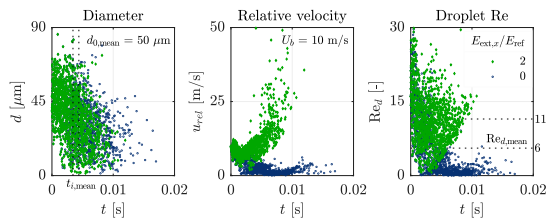


**Fig. 14.** Instantaneous distribution of the droplet size, relative velocity and Reynolds number versus the droplet age obtained from LES including evaporation for a polydisperse spray. – Case C.
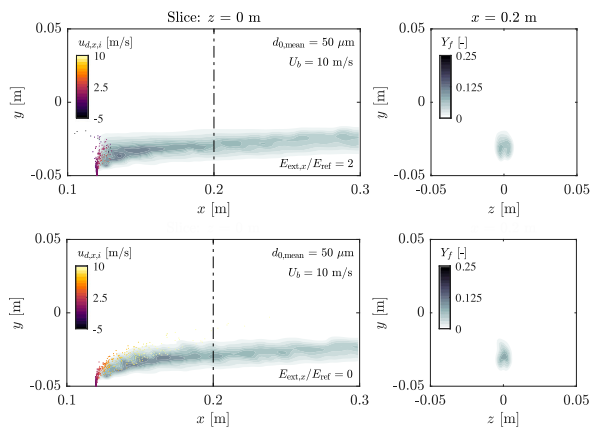


**Fig. 15.** Instantaneous fuel vapour mass fraction, $Y_f$, in the mid-plane and in an axial plane obtained from LES including evaporation for a polydisperse spray. Top: external electrostatic field in the $x$-direction. Bottom: no electrostatic forces. The corresponding droplet distribution is coloured by the axial droplet velocity, $u_{d,x,i}$, and was sampled in the range $\pm 5 \times 10^{-4}$ m perpendicular to the mid-plane. – Case C.

maximum gradients and concentrations. This is also visible in the mid-plane, especially when the region approximately 70 mm downstream of the injection location is analysed. Higher levels of turbulence in the continuous phase can be observed, as eluded to in the previous section. The root mean square of the gas-phase velocity was spatially averaged in both the mid-plane and the axial plane, showing an increase of more than 42% and 28%, respectively, when stabilising the droplet cloud. In practical applications, the mixing can be further enhanced by increasing the level of turbulence after complete evaporation (e.g., by means of turbulators).

The '*targeted evaporation*' concept can also be extended to polydisperse sprays (Case C). The operating condition investigated here is almost identical to Case B, however, a spray opening angle and initial droplet size distribution equal to Case A are utilised to produce the polydisperse spray (cf. Table 1). The results presented in Fig. 13 demonstrate that electrostatic forces can be exploited to control the droplet location and release of fuel vapour in polydisperse sprays. Analogous to the findings determined with a monodisperse spray, faster

evaporation and an increase of the residence time in the region close to the injection, i.e. lower axial penetration, are observed. The mean droplet age (parcel average), $t_{i,\mathrm{mean}}$, of the full spray cloud quantified in Fig. 14 decreases by almost 25% from 4.4 ms to 3.4 ms (vertical dashed lines). Although not as obvious as in the monodisperse spray results, Fig. 15 shows that completion of the evaporation process further upstream again leads to a slightly more uniformly distributed fuel vapour concentration.

The above findings indicate that a controlled local release of fuel vapour has been achieved, successfully demonstrating the feasibility of the proposed '*targeted evaporation*' concept. Moreover, despite neglecting the effects of turbulence, the deterministic model provides a reasonable prediction of the mean droplet trajectory, which can be further improved by including evaporation.

## 4. Summary and conclusions

The use of EHD-based technologies in civil aviation will become increasingly feasible with the anticipated introduction of future hybrid thermal–electric aero-engines. It is under this premise that the present work explored the application of electrostatic forces for the spatial control of evaporating fuel droplets. LES was performed on an electrospray in cross-flow, which combines the use of an external electrostatic field with the injection of electrically charged fuel droplets. The results showed that a modulation of the droplets' mean trajectory is achievable using electrostatic fields below the breakdown threshold of air and with droplet charges typical of current electrospray technologies. It was also found that the effectiveness of the electrostatic force decreases considerably with increasing bulk flow velocities. A deterministic model was presented to complement the numerical simulations and to provide a preliminary design tool. The model enabled a separation of the effects of turbulence, evaporation and repulsion via comparisons with bin-averaged LES data.

By orienting the external electrostatic field in the streamwise direction, it was demonstrated that it is possible to confine the droplets in the vicinity of the injection location and obtain quasi-infinite droplet residence times at moderate bulk flow velocities. This is a result of a balance between the drag and electrostatic force, which was achieved with negligible power requirements. The effective time available for droplet evaporation within a finite-length fuel–air mixing region can thereby be increased significantly, suggesting that the combination of electrosprays and external electrostatic fields could be a viable technology to obtain prevapourised fuel in compact injection systems. Moreover, the location of the fuel vapour release in both monodisperse and polydisperse sprays may be controlled by modulating the external electrostatic field, therefore achieving a '*targeted evaporation*'. The increased relative velocity between the droplets and the bulk flow, as a consequence of the stagnating spray cloud, also leads to higher droplet Reynolds numbers with two main benefits: enhanced evaporation rates (a reduction of the total evaporation time by 30% was determined) and stronger droplet dispersion due to higher turbulence intensities in the continuous phase. The dispersion of droplets is further enhanced via the repulsion forces acting between the equally charged fuel droplets. In total, a fourfold increase of the droplet dispersion was observed. Overall, these effects enable a quicker, more efficient fuel–air mixing process resulting in more homogeneous reactant mixtures and a potentially improved control and reduction of pollutant emissions.

### Declaration of competing interest

The authors declare that they have no known competing financial interests or personal relationships that could have appeared to influence the work reported in this paper.

### Data availability

The authors are unable or have chosen not to specify which data has been used.

## Acknowledgements

## References

Abramzon, B., Sirignano, W., 1989. Droplet vaporization model for spray combustion calculations. Int. J. Heat Mass Tran. 32 (9), 1605–1618.

Aggarwal, S.K., Tong, A.Y., Sirignano, W.A., 1984. A comparison of vaporization models in spray calculations. AIAA J. 22 (10), 1448–1457.

Ahmed, T., Kourmatzis, A., Masri, A.R., 2021a. Atomization behaviour of a hybrid air-blast-electrostatic atomizer for spray combustion. Fuel 288, 119716.

Ahmed, T., Kourmatzis, A., Pham, P., Masri, A., 2018. Droplet evaporation modeling of electrified fatty acid methyl esters. Fuel 231, 244–252.

Ahmed, T., Kourmatzis, A., Singh, G., Masri, A.R., 2021b. Turbulent spray flames of kerosene issuing from a hybrid electrohydrodynamic-air-blast atomiser. Combust. Flame 111573.

Al-Nuaimi, O.A., Kyritsis, D.C., 2019. Bioalcohol electrosprays for practical propulsion systems. J. Energ. Eng. 145 (1), 04018069.

Bailey, A.G., 1998. The science and technology of electrostatic powder spraying, transport and coating. J. Electrostat. 45 (2), 85–120.

Baroutaji, A., Wilberforce, T., Ramadan, M., Olabi, A.G., 2019. Comprehensive investigation on hydrogen and fuel cell technology in the aviation and aerospace sectors. Renew. Sust. Energ. Rev. 106, 31–40.

Beaton, C.F., Hewitt, G.F., 1989. Physical Property Data for the Design Engineer. Hemisphere Publishing Corp.

Brelje, B.J., Martins, J.R., 2019. Electric, hybrid, and turboelectric fixed-wing aircraft: A review of concepts, models, and design approaches. Prog. Aerosp. Sci. 104, 1–19.

Brewer, G.D., 2017. Hydrogen Aircraft Technology. Routledge.

Crowley, J.M., 1995. Electrostatic fundamentals. In: Handbook of Electrostatic Processes. CRC Press, pp. 1–23.

Doyle, A., Moffett, D., Vonnegut, B., 1964. Behavior of evaporating electrically charged droplets. J. Colloid Sci. 19 (2), 136–143.

Fredrich, D., Giusti, A., 2022. Numerical investigation of multi-component droplet evaporation and autoignition for aero-engine applications. Combust. Flame 241, 112023.

Fredrich, D., Miniero, L., Pandey, K., Jones, W.P., Noiray, N., Giusti, A., 2022. Large eddy simulation of a reacting kerosene spray in hot vitiated cross-flow. Flow Turbul. Combust.

Galliker, P., Schneider, J., Eghlidi, H., Kress, S., Sandoghdar, V., Poulikakos, D., 2012. Direct printing of nanostructures by electrostatic autofocussing of ink nanodroplets. Nature Commun. 3 (1), 1–9.

Gnadt, A.R., Speth, R.L., Sabnis, J.S., Barrett, S.R., 2019. Technical and environmental assessment of all-electric 180-passenger commercial aircraft. Prog. Aerosp. Sci. 105, 1–30.

Higuera, F.J., Tejera, J.M., 2017. Vaporization and gas-phase combustion of electrosprayed heptane in a small chamber. Combust. Flame 177, 144–154.

International Air Transport Association, available at https://www.iata.org/en/programs/environment/sustainable-aviation-fuels/.

Jenny, P., Roekaerts, D., Beishuizen, N., 2012. Modeling of turbulent dilute spray combustion. Prog. Energy Combust. Sci. 38 (6), 846–887.

Kelly, A., 1984. The electrostatic atomization of hydrocarbons. J. Inst. Energy 57 (431).

Kourmatzis, A., 2017. Sensitivities in the modeling of electrostatically charged droplet evaporation and combustion. J. Energ. Eng. 143 (3), 04016060.

Kourmatzis, A., Shrimpton, J., 2014. Electrohydrodynamic inter-electrode flow and liquid jet characteristics in charge injection atomizers. Exp. Fluids 55 (3), 1–13.

Kyritsis, D.C., 2020. Electrostatically manipulated flames for compact heat generation. US Patent 10, 677, 455 B2.

Kyritsis, D.C., Coriton, B., Faure, F., Roychoudhury, S., Gomez, A., 2004. Optimization of a catalytic combustor using electrosprayed liquid hydrocarbons for mesoscale power generation. Combust. Flame 139, 77–89.

Kyritsis, D.C., Guerrero-Arias, I., Roychoudhury, S., Gomez, A., 2002. Mesoscale power generation by a catalytic combustor using electrosprayed liquid hydrocarbons. Proc. Combust. Inst. 29 (1), 965–972.

Lawton, J., Weinberg, F.J., 1969. Electrical Aspects of Combustion. Oxford University Press.

Lefebvre, A.H., McDonell, V.G., 2017. Atomization and Sprays. CRC Press.

Li, Z., Long, Y., Zhong, J., 2021. Stability and decay of surface electrostatic charges in liquids. Nano Energy 81, 105618.

Liu, Y., Sun, X., Sethi, V., Nalianda, D., Li, Y.-G., Wang, L., 2017. Review of modern low emissions combustion technologies for aero gas turbine engines. Prog. Aerosp. Sci. 94, 12–45.

Masri, A., 2021. Challenges for turbulent combustion. Proc. Combust. Inst. 38 (1), 121–155.

Mehta, R.N., Chakraborty, M., Parikh, P.A., 2014. Nanofuels: Combustion, engine performance and emissions. Fuel 120, 91–97.

Miller, R., Harstad, K., Bellan, J., 1998. Evaluation of equilibrium and non-equilibrium evaporation models for many-droplet gas-liquid flow simulations. Int. J. Multiph. Flow 24 (6), 1025–1055.

Mizeraczyk, J., Podlinski, J., Niewulis, A., Berendt, A., 2013. Recent progress in experimental studies of electro-hydrodynamic flow in electrostatic precipitators. In: J. Phys.: Conf. Ser.. 418, IOP Publishing, 012068.

Mongia, H., 2003. TAPS: A fourth generation propulsion combustor technology for low emissions. In: AIAA International Air and Space Symposium and Exposition: The Next 100 Years. p. 2657.

Putnam, A., 1961. Integrable form of droplet drag coefficient. ARS J. 31, 1467–1468.

Rayleigh, L., 1882. XX. On the equilibrium of liquid conducting masses charged with electricity . Lond. Edinb. Dublin Philos. Mag. J. Sci. 14 (87), 184–186.

Rigit, A., Shrimpton, J.S., 2009. Estimation of the diameter–charge distribution in polydisperse electrically charged sprays of electrically insulating liquids. Exp. Fluids 46 (6), 1159–1171.

Shrimpton, J., 2005. Dielectric charged drop break-up at sub-Rayleigh limit conditions. IEEE Trans. Dielectr. Electr. Insul. 12 (3), 573–578.

Shrimpton, J., 2009. Charge Injection Systems: Physical Principles, Experimental and Theoretical Work. Springer Science & Business Media.

Shrimpton, J.S., Laoonual, Y., 2006. Dynamics of electrically charged transient evaporating sprays. Internat. J. Numer. Methods Engrg. 67 (8), 1063–1081.

Shrimpton, J., Yule, A., 1999. Characterisation of charged hydrocarbon sprays for application in combustion systems. Exp. Fluids 26 (5), 460–469.

Soldati, A., 2000. On the effects of electrohydrodynamic flows and turbulence on aerosol transport and collection in wire-plate electrostatic precipitators. J. Aerosol Sci. 31 (3), 293–305.

Tang, K., Gomez, A., 1996. Monodisperse electrosprays of low electric conductivity liquids in the cone-jet mode. J. Colloid Interface Sci. 184 (2), 500–511.

Uhm, H.S., 1999. Properties of plasmas generated by electrical breakdown in flames. Phys. Plasmas 6 (11), 4366–4374.

Wallis, G.B., 2020. One-dimensional two-phase flow. Courier Dover Publications.

Walther, D.C., Ahn, J., 2011. Advances and challenges in the development of power-generation systems at small scales. Prog. Energy Combust. Sci. 37 (5), 583–610.

Wei, Y., Deng, W., Chen, R.-H., 2016. Effects of insoluble nano-particles on nanofluid droplet evaporation. Int. J. Heat Mass Transfer 97, 725–734.

Yamamoto, T., Velkoff, H.R., 1981. Electrohydrodynamics in an electrostatic precipitator. J. Fluid Mech. 108, 1–18.

Yuen, M.C., Chen, L.W., 1976. On drag of evaporating liquid droplets. Combust. Sci. Technol. 14 (4–6), 147–154.

Yule, A., Shrimpton, J., Watkins, A., Balachandran, W., Hu, D., 1995. Electrostatically atomized hydrocarbon sprays. Fuel 74 (7), 1094–1103.

Zhang, C., Hui, X., Lin, Y., Sung, C.-J., 2016. Recent development in studies of alternative jet fuel combustion: Progress, challenges, and opportunities. Renew. Sust. Energ. Rev. 54, 120–138.